Key Points:
- Sediment core from the Pacific-Antarctic Ridge records discrete layer of volcaniclastics preceding glacial Termination 2
- Morphology and geochemistry of glass shards are consistent with axial volcanic eruptions
- Glass shards transported to core site via buoyant plume that occupied most of the water column above the ridge axis

Correspondence to:
D. C. Lund,
david.lund@uconn.edu

Anomalous Pacific-Antarctic Ridge Volcanism Precedes Glacial Termination 2

David C. Lund[1] [ID]**, Emily I. Seeley[1], Paul D. Asimow[2]** [ID]**, Madeline J. Lewis[2], Sarah E. McCart[1], and Annalisa A. Mudahy[1]**

[1]Department of Marine Sciences, University of Connecticut, CT, USA, [2]Division of Geological and Planetary Sciences, California Institute of Technology, CA, USA

Abstract We present results from a well-dated sediment core on the Pacific-Antarctic Ridge (PAR) that document a ∼15 cm thick layer of basaltic ash shards that precedes the penultimate deglaciation (Termination 2). The glasses have MORB composition consistent with an axial source and their morphologies are typical of pyroclastic deposits created by submarine volcanism. The ash layer was deposited ∼7 km from the PAR axis, a distance that implies buoyant plumes lofted debris high into the water column with subsequent fallout to the core location. We infer plume rise height using grain settling velocities, the water depth at the core location, and deep ocean current speeds from ARGO floats. Rise heights of 1.5 km or less require unrealistically large current speeds to transport grains to the core site. Instead, the data are consistent with a plume rise height of at least 2 km, implying that T2 was an interval of anomalous volcanism along this segment of the PAR. The timing and duration of the ash deposit is consistent with glacial-interglacial modulation of ridge magmatism. Volcaniclastic records from additional locations will be necessary to assess whether the PAR record is a rare find or it is representative of mid-ocean ridge volcanism during glacial terminations.

1. Introduction

The growth and decay of Pleistocene ice sheets repeatedly transferred ∼4×10^{19} kg of water between the Earth's oceans and continents. Ice sheet retreat and crustal unloading appears to trigger subaerial volcanism at high latitudes (Huybers & Langmuir, 2009; Maclennan et al., 2002). Similarly, ice sheet growth and falling sea level should promote submarine volcanism by enhancing decompression melting below mid-ocean ridges (Huybers & Langmuir, 2009; Lund & Asimow, 2011). Ridge flank bathymetry appears to display Milankovitch frequencies (Crowley et al., 2015; Tolstoy, 2015), but the connection between sea level and seafloor bathymetry is a matter of ongoing debate involving complexities of seafloor tectonic development that are somewhat separate from the time-dependence of mid-ocean ridge magmatic flux (Goff, 2015; Olive et al., 2015). Alternative proxies will therefore be useful for determining whether sea level modulates mid-ocean ridge magmatism and the timing of any associated magmatic anomalies at the ridge crest. Recently published sediment records suggest the flux of hydrothermal metals from the East Pacific Rise (EPR) varied on glacial-interglacial timescales, peaking during glacial Terminations 1 and 2 (Lund et al., 2016). Records from the Mid-Atlantic Ridge and Juan de Fuca Ridge are also consistent with enhanced hydrothermal fluxes during Termination 1 (Costa et al., 2017; Middleton et al., 2016).

In this paper, we propose that an additional proxy, sediment-hosted basaltic glasses, can be used to assess Milankovitch-scale changes in mid-ocean ridge magmatism. Pyroclastic ash deposits are the unequivocal product of submarine volcanism and they can be dated using oxygen isotope analyses of foraminifera within the same sediment. Pyroclastic glasses are routinely found within a few kilometers of mid-ocean ridges, suggesting that mildly explosive (i.e., Strombolian) submarine volcanism is more pervasive than previously thought (Clague et al., 2003; Clague et al., 2009; Portner et al., 2015; Sohn et al., 2008). In a recent study, basaltic glass shards from a well-dated sediment core were used to infer long-term changes in melt composition on the Juan de Fuca Ridge (Ferguson et al., 2017). Here we report the discovery of an ash layer in core OC170-26-159, near the Pacific-Antarctic Ridge (PAR) (Figure 1). The glassy lava fragments are interspersed with foraminifera whose isotopic composition records glacial Termination 2 (T2) (Figure 2). The angular and curved fluidal morphologies of the fragments are consistent with volatile-rich submarine
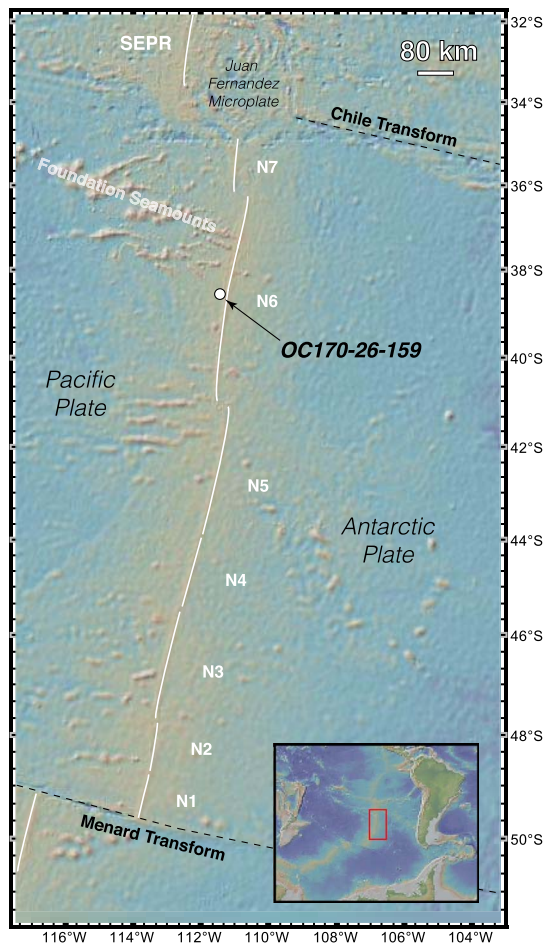
Figure 1. Map of the Pacific-Antarctic Ridge including the location of core OC170-26-159 (38.967°S, 111.350°W, 2754 m water depth) and segments N1-N7 (white lines) (Briais et al., 2009; Klingelhoefer et al., 2006). The core site is located 13.5 ± 1.5 km from the PAR axis. The available bathymetry data indicate the nearest seamount is located approximately 25 km west of the core site. Map generated using GeoMapApp (Ryan et al., 2009).

eruptions (Clague et al., 2009). The T2 layer was deposited when the core site was 7 km off-axis, farther than any submarine ash layer documented in the published literature. The location and thickness of the layer suggests T2 was an anomalous interval of volcanic activity that lofted pyroclastic debris high into the water column with subsequent fallout to ridge flank locations.

Below we present the analytical and modeling results that point to an axial source for the T2 layer. The discovery of this anomalous interval in the eruptive history of the PAR is notable in its own right, but we also consider the implications for the local axial magma system through the penultimate glacial cycle. Although it is possible that this deposit will remain unique, it may have broader implications for testing the sea level hypothesis if other examples can be found; hence, we also discuss the probability of finding similar ash layers that would support generalization of our results to other ridges.

2. Methods

### 2.1. Oxygen Isotope Analyses and Age Model Construction

Sediment samples from core OC170-26-159 were frozen for 24 hours and freeze-dried for ∼48 h. Subsamples for foraminiferal analysis were washed over a 150 μm sieve using distilled water and oven-dried for 30 min at 70°C. Oxygen isotope ratios ($\delta^{18}O$) were measured on both planktonic and benthic foraminifera using a Finnigan MAT-253 isotope ratio mass spectrometer coupled to a Kiel IV automated carbonate device. Planktonic analyses were based on 6–7 individual *G. ruber* shells (> 250 μm size fraction), while the benthic analyses were based on individual shells of *C. wuellerstorfi* (n = 43) *and C. kullenbergi* (n = 8) (> 250 μm in both cases). Benthic samples run at the University of Michigan (n = 51) were converted to Vienna Pee-Dee Belemnite (VPDB) using NBS-19 (n = 8, $\delta^{18}O = -2.16 \pm 0.05$ ‰, $\delta^{13}C = 1.91 \pm 0.05$ ‰) and cross-checked using Atlantis II (n = 7, $\delta^{18}O = 3.50 \pm 0.05$ ‰, $\delta^{13}C = 0.79 \pm 0.04$ ‰) (Ostermann & Curry, 2000). Planktonic samples run at Georgia Tech (n = 60) were converted to VPDB via NBS-19 (n = 2, $\delta^{18}O = -2.16 \pm 0.02$ ‰, $\delta^{13}C = 1.94 \pm 0.004$ ‰), NBS-18 (n = 5, $\delta^{18}O = -23.08 \pm 0.16$ ‰, $\delta^{13}C = -5.02 \pm 0.03$ ‰), and an in-house standard similar to NBS-19 (n = 14, $\delta^{18}O = -2.04 \pm 0.05$ ‰, $\delta^{13}C = 2.15 \pm 0.02$ ‰). The age model for OC170-026-159 was determined by correlating the planktonic and benthic $\delta^{18}O$ time series to the benthic stack of Lisiecki and Raymo (2005). Approximate calendar age uncertainty for each tie point is ±3 kyr. Age control points were linearly interpolated to produce the age model for intervening samples.

2.2. Sediment Digestions

Dried, ground samples underwent a four-step microwave acid digestion protocol following Morford and Emerson (1999). We ground 500 mg of bulk sediment from each depth, 200 mg of which was placed in a 60 mL Savillex® Teflon digestion vessel with concentrated 5:2 HF/HNO₃ solution. The vessels were refluxed in a microwave and evaporated to dryness. Each sample then underwent reflux in 3:1 HCl/HNO₃, evaporation, reflux in 2:1 30% H₂O₂/HNO₃, evaporation, and finally 2 h reflux in 5% HNO₃. During method development, incomplete dissolution of the external standard motivated an additional ∼8 h HCl/HNO₃ reflux to ensure dissolution of both standards and unknowns. Digested samples were quantitatively transferred into 125 mL Nalgene bottles and diluted up to 100 mL with 2% HNO₃. All acids used were trace metal grade (Optima™).

2.3. Bulk Sedimentary Metal Concentrations

Bulk sediment concentrations of Ti and Al were determined at UCONN Avery Point using a Thermo Element 2 inductively coupled plasma mass spectrometer (ICP-MS) paired with a ESI SC-2 DX auto-sampler. We quantified elemental concentrations using standard addition of matrix-matched spike solutions,
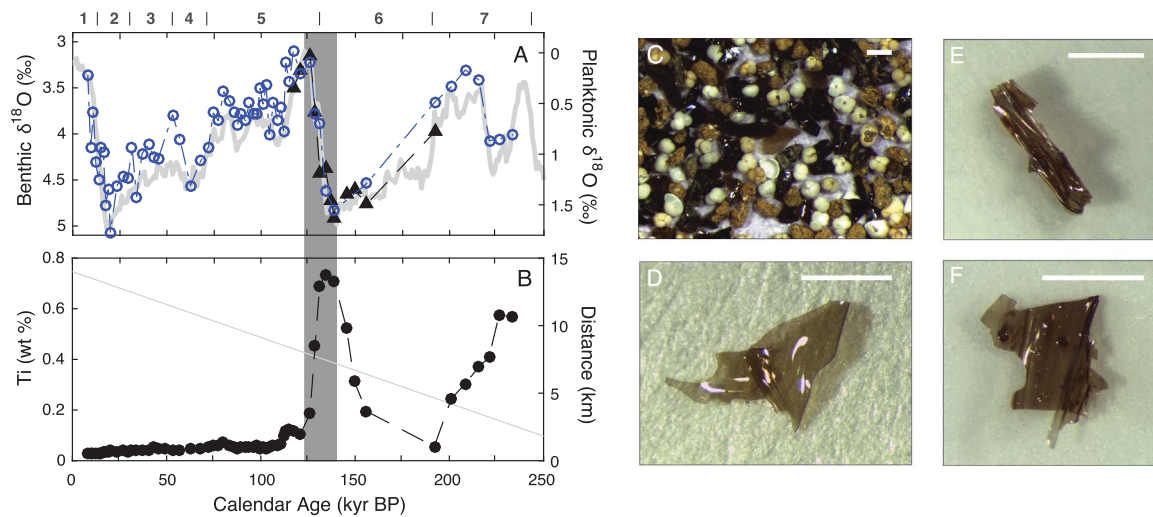
Figure 2. Stable isotope and titanium concentration results for core OC170-26-159. (**a**) Planktonic $\delta^{18}O$ (blue circles) and average benthic $\delta^{18}O$ (black triangles) compared to the global benthic $\delta^{18}O$ stack of Lisiecki and Raymo (2005) (gray line). Note that 0.4 per mil has been added to the OC170-26-159 benthic data to facilitate comparison to the global stack. Marine Isotope Stages 1–7 are noted on the upper x-axis. (**b**) Titanium concentrations for core OC170-26-159 (black circles) and core distance from the ridge axis versus time (thin gray line). Titanium concentrations during glacial Termination 2 (dark gray vertical bar) are ~15x higher than in the younger part of the core. Core distance from the ridge axis is based on the modern distance of 13.5 km and a half-spreading rate of 49 mm/yr (www.ldeo.columbia.edu/~menke/plates.html). (**c**) Raw sample from the T2 layer showing foraminifera, blocky glass shards, and consolidated hemipelagic mud. (**d–f**) Examples from the T2 layer showing the curved limu o Pele morphology characteristic of submarine volcanism. The scale bar in each image is 250 μm.

gravimetrically prepared using standards from Accustandard (http://www.accustandard.com/). Spiked samples were diluted to 1/15 in 2% HNO_3 prior to analysis. Internal spikes (^{89}Y and ^{115}In) were added to select samples to monitor quantitative transfer throughout digestion and analysis.

Analytical precision and accuracy were assessed through repeated digestion, measurement, and analysis of the certified standard MESS-4 (National Research Council, Canada) (n = 22). The average Ti concentration for MESS-4 was 0.38 $\pm$ 0.02% (2σ), within analytical uncertainty of the certified value, 0.36 $\pm$ 0.03% (2σ). Aluminum concentrations averaged 7.23 $\pm$ 0.47% (2σ), slightly lower than the certified value of 7.91 $\pm$ 0.20% (2σ). Aluminum results were used only to qualitatively cross-check titanium, the preferred indicator of basaltic inputs, because seawater scavenging can be a significant source of aluminum in hydrothermal sediments (Dunk & Mills, 2006).

2.4. Major and Trace Elemental Analyses of Basaltic Glass

Major elements (Si, Ti, Al, Fe, Mn, Mg, Ca, Na, K, and Cl) of 67 glass shards were analyzed using Caltech's JEOL JXA-8200 electron microprobe, operating at 15 kV and 10 nA with a 10 μm diffuse beam and the CIT-ZAF matrix correction program. Counting times were 30 s on-peak and 15 s at each background location for all elements, with Na, K, and Cl in the first pass. Standards were synthetic forsterite, fayalite, Mn-olivine, anorthite, TiO_2, and Cr_2O_3 plus natural Amelia albite, Asbestos microcline, and sodalite. All elements measured in VG2 basalt glass were within <2% relative of accepted concentrations. Five or more spots were measured on each glass shard. Points contaminated by olivine or plagioclase microphenocrysts were discarded; reported concentrations and uncertainties are averages and 1σ of remaining analyses on single shards.

H_2O and CO_2 species concentrations were determined by transmission Fourier Transform Infrared Spectroscopy (FTIR) on doubly polished shards < 100 μm thick (measured by digital micrometer) with a Thermo-Nicolet iS50 FTIR Spectrometer (KBr beam splitter; InGaAs detector) and Nicolet Continuum Infrared Microscope. Spectra (1300–6000 cm^{-1}) were averaged over 200–300 scans. Two to four 25–40 μm spots were measured on each shard. Absorption intensities were determined for OH and H_2O peaks centered at 3500 and 1630 cm^{-1} and carbonate peaks centered at 1430 and 1515 cm^{-1}. To remove background from the low intensity CO_2 peaks, we subtracted the spectrum of a quantitatively degassed basalt glass. Volatile species concentrations were obtained from peak heights and the Beer-Lambert law with molar absorptivities:

63 L/(mol·cm) for the 3500 cm^{-1} peak, 25 L/(mol·cm) for the 1630 cm^{-1} peak (Dixon et al., 1995), and 375 L/(mol·cm) for the 1415 and 1530 cm^{-1} peaks (Fine & Stolper, 1985). Density was estimated as 2.89 g/cm^3 using Glass Density Calc v3.2. Concentrations and uncertainties are reported as averages and 1σ of the 2 to 4 analyses on each shard.

Trace elements in the glass shards were measured by laser-ablation ICP-MS at the Caltech Environmental Analysis Center. With a New Wave Research UP 193 Solid State Laser System (193 nm wavelength, 3 ms pulse width) attached to an Agilent 8800 ICP-MS, we analyzed, in spectrum mode, ^{29}Si, ^{43}Ca, ^{44}Ca, ^{47}Ti, ^{85}Rb, ^{88}Sr, ^{89}Y, ^{90}Zr, ^{93}Nb, ^{133}Cs, ^{137}Ba, ^{138}Ba, ^{139}La, ^{140}Ce, ^{141}Pr, ^{146}Nd, ^{147}Sm, ^{151}Eu, ^{157}Gd, ^{159}Tb, ^{163}Dy, ^{165}Ho, ^{166}Er, ^{169}Tm, ^{172}Yb, ^{175}Lu, ^{178}Hf, ^{181}Ta, ^{208}Pb, ^{232}Th, and ^{238}U. One replicate with 90 sweeps and 0.0501s integration time for all masses except ^{44}Ca (0.1000 s) gave total acquisition time of 11 s. Washout delay (7 s) and gas blank (10 s) ensured return to background signals between analyses. 100 μm spots were pre-ablated (1 s, 45% laser power, 10 Hz repetition rate; He option gas flow 8 mL/min) before each analytical ablation (10 s, 35 μm spot, 80% laser power). ICP-MS parameters were 1550 W RF power and 1 L/min Ar carrier gas flow. Before and after unknowns, six spots were ablated on primary reference standard NIST 612 glass. ^{29}Si content by electron microprobe was used as internal standard. Three to six spots were analyzed on each shard, depending on size; reported uncertainties for each shard are 1σ of the calculated concentrations.

2.5. Grain Size and Settling Velocities

Grain size distributions for the glass shards were determined with sieves stacked in descending order (500, 250, 125, 63, and 37 μm). Approximately 500 mg of each sample was rinsed in tap water until only basalt fragments and foraminifera were visible. Each size fraction was then repeatedly oven dried at 70°C, acidified using 5% HNO$_3$, washed, and dried until only glass remained. Some clay adhered to the shards but the contribution to total weight was negligible; more aggressive removal might have caused breakage and affected the size fraction results.

To compare the PAR results to the Gorda Ridge data from Clague et al. (2009), it was necessary to translate their visual estimates of glass percentage into percent basalt per size fraction relative to the total glass in each sample. For example, Gorda Ridge sample T887-PC55 had 0.953 g total sediment in the 125–250 μm size fraction and, by visual estimate, 20% glass. That yields 0.19 g glass, assuming similar densities for the glass and other sedimentary components, which is primarily quartz sand (D. Clague, personal communication). The Gorda Ridge samples were recovered at depth of $\sim$3200 m, below the carbonate compensation depth (CCD), so foraminifera were a negligible component of the sediment. Clague et al. (2009) summed the masses for each size fraction (63–125 μm, 125–250 μm, 250–500 μm, and >500 μm) to determine total mass of glass for each sample. We simply divided the mass for each fraction by the total mass to determine percentages. To check the visual estimates, we summed the percentages; those samples where the total exceeded 90% (n = 117) were retained while those less than 90% (n = 12) were excluded. To assess grain size distribution versus distance from the lava flow, the Gorda Ridge data were grouped into bins by approximate distance from the source: >1600 g/m^2 (<0.5 km), 400–1600 g/m^2 (0.5.−1.0 km), 100–400 g/m^2 (1–2 km), 50–100 g/m^2 (2–3 km), and < 50 g/m^2 (> 3 km). Clague et al. (2009) did not estimate glass content in the terrigenous-dominated 36–63 μm size fraction, so the Gorda Ridge coarse fraction percentages may be biased slightly high relative to the PAR results.

Grain settling velocities for the PAR glasses were determined for three size fractions: 125–150 μm, 150–212 μm, and 212–250 μm. In each case, 50 blocky, equant grains (the dominant morphology) were dropped in a 40 cm tall by 30 cm diameter cylindrical tank of seawater collected at UCONN Avery Point. The seawater was cooled to 0°C to approximate the temperature and viscosity of the deep Southeast Pacific during glacial maxima (Adkins et al., 2002). Individual grains were tracked by eye as they fell against a white background. Settling times were determined by stopwatch and the resulting values were used in combination with the tank height to calculate settling velocities. Settling velocities for the upper and lower halves of the water column were compared to ensure terminal velocity had been reached; the results were within one standard error for all size fractions.
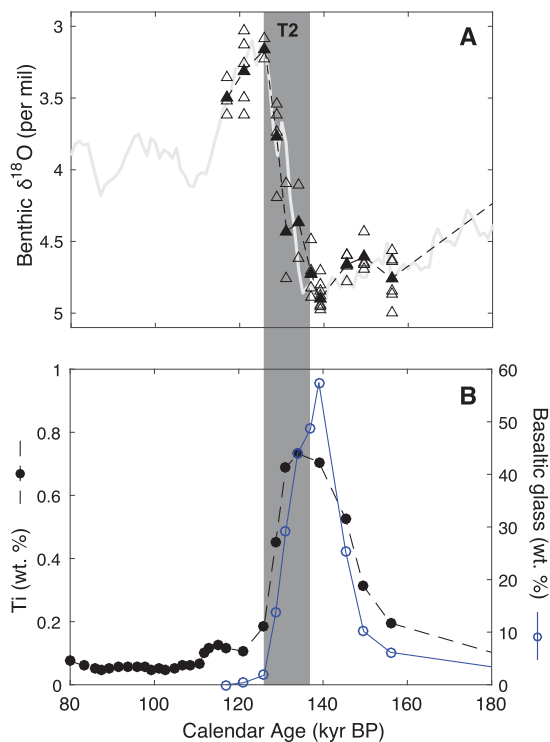
2.6. Current Speeds

Estimates of current speed are required to assess dispersal of volcaniclastic grains in the deep ocean. The range of likely deep ocean current speeds in vicinity of the core site (38.97°S, 111.35°W, 2754 m water

depth) was constrained using ARGO float data from 30°S to 45°S and 100°W to 120°W (Lebedev et al., 2007). ARGO data constrain current speeds at depth because the floats spend 95% of their time at preselected isobaric surfaces (Lebedev et al., 2007). These so-called "parking depths" are typically 1000 or 2000 db. We extracted 2200 discrete estimates of current speed in the region: 1866 at 1000 db and 334 at 2000 db. The estimated mean uncertainty of ARGO-derived deep current velocities for the global ocean is 0.5 cm/s, compared to a mean velocity of 5 cm/s. The ~10% uncertainty is due to geostrophic currents, Ekman transport, and inertial oscillations during descending and ascending phases of the float cycle (Lebedev et al., 2007).

3. Results

3.1. Oxygen Isotope, Titanium, and Basalt Concentrations

The planktonic $\delta^{18}O$ time series for OC170-26-159 records marine oxygen isotope stages 1–6, indicating there has been continuous sediment deposition at the core site over the past 160 kyr (Figure 2a). The shorter benthic $\delta^{18}O$ time series, focused on the T2 interval, also indicates continuous accumulation at ~1 cm/kyr. The sedimentation rate from 160 to 190 kyr BP was considerably slower (0.1 cm/kyr), while prior to 190 kyr BP it was ~0.3 cm/kyr. The apparent minimum in sedimentation rate from 160 to 190 kyr BP may indicate a hiatus at ~138 cm, or 10 cm below the T2 interval. The $\delta^{18}O$ data in the deepest part of the core are consistent with MIS 7 but the stratigraphic quality is lower so the timing of events older than 160 kyr BP is uncertain.
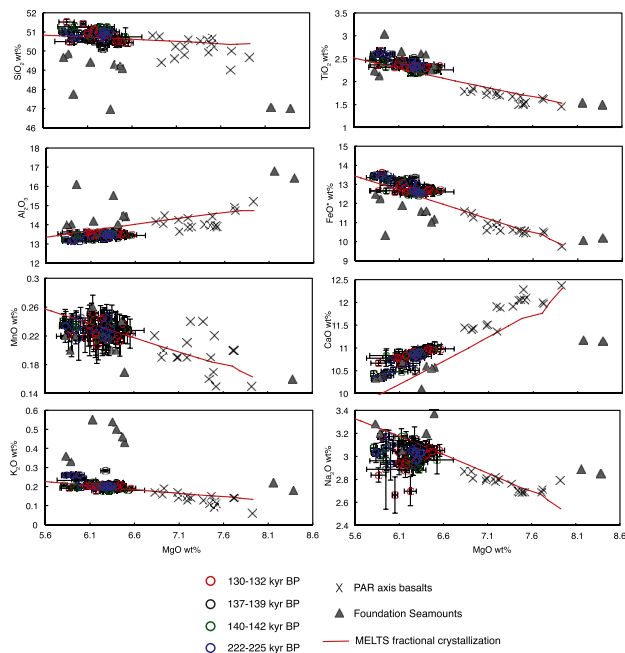
The T2 ash layer is apparent in the washed sediment (Figure 2c), titanium concentration (Figure 2b), and weight percent basaltic glass data (Figure 3). Glass concentrations began to increase prior to T2, peaked early in T2, and returned to background by the end of T2 (Figure 3). The majority of glasses in the T2 layer (>90%) exhibit blocky morphology (Figure 2c) but curved fluidal shapes (limu o Pele) are also present (Figures 2d–2f). A second, weaker maximum in Ti concentration occurs deeper in the core (Figure 2b). Given a half-spreading rate of 49 mm/yr (www.ldeo.columbia.edu/~menke/plates.html), the T2 ash was deposited when the core site was approximately 7 km from the PAR axis. The deeper ash layer was deposited when the core site was 2–3 km off-axis (Figure 2b).

3.2. Glass Shard Geochemistry

Major oxide concentrations for all the basaltic glass shards (Figure 4) form a single population regardless of age (MgO = 6.2 ± 0.3%, 2σ), with variability comparable to that for individually mapped axial lava flows (Rubin et al., 2001). The shards have MgO contents lower than those of basalts collected from the nearest segment of the modern PAR axis (MgO 6.8–7.9 wt %) (Freund et al., 2013; Hekinian et al., 1999). Variability among shards forms linear trends in MgO variation diagrams, continuous with trends through the axial compositions. MgO contents in Foundation Seamount glasses span 5.8–8.4 wt % and they differ from the shards and axial samples in means, slopes, and degrees of scatter in oxide concentrations (Figure 4).

Incompatible trace elements (Figure 5) are enriched in the glass shards relative to modern axial basalts. However, as with the major elements, the shard population falls along common linear trends with the axial basalts and they are much more homogeneous than the few scattered samples from the Foundation Seamounts. Sr is only slightly enriched in the glass shards relative to axial basalts because of plagioclase fractionation.

We calculated the liquid line of descent from the most primitive axial basalt (Table 1; all major elements and those trace elements with available data) using the MELTS model (Ghiorso & Sack, 1995) at a constant pressure of 900 bars and oxygen fugacity controlled two log units below the QFM buffer (conditions that create the best match to MORB fractionation in MELTS; Asimow et al., 2004), yielding

Figure 3. Benthic stable isotope, titanium, and glass concentration results for 80–180 kyr BP. (a) Average benthic $\delta^{18}O$ (filled triangles) compared to the global benthic $\delta^{18}O$ stack of Lisiecki and Raymo (2005) (gray line). Also shown are the $\delta^{18}O$ results for individual benthic foraminifera (open triangles). Note that 0.4 per mil has been added to the benthic data to facilitate comparison to the global stack. The gray vertical bar represents the approximate time interval of T2. (b) Titanium (black circles) and glass concentrations (blue circles). Glass concentrations are for the >38 μm size fraction. Note that both Ti and basalt levels began to increase prior to T2.

Figure 4. Major element oxide compositions for the basaltic glass shards in core OC170-26-159 at four different age intervals. The glass shards are consistently more evolved than basalts erupted from the current ridge axis (black X's) (compositions from Hekinian et al., 1999, and Freund et al., 2013) and define a single population despite different depositional ages. The population lies along a liquid line of descent (red line) determined using the MELTS thermodynamic model (Asimow & Ghiorso, 1998; Ghiorso & Sack, 1995) with a starting composition similar to basalts erupted from the ridge axis and pressure and fO_2 values consistent with mid-ocean ridge conditions. Compositions from the proximal Foundation Seamounts (gray triangles) (Hekinian et al., 1997) are included for comparison; the fractionation trend defined by the glass shards is not consistent with this neighboring magmatic system.

a trend through the axial glass and glass shard compositions (Figures 4 and 5). The fit of the model suggests the glass shards are related to the axial magmatic system by fractional crystallization and represent more evolved members of the same sequence. The modeled fractionation occurred at temperatures from 1190 to 1150°C, corresponding to a temperature and composition-dependent increase in magma viscosity from 23 Pa·s to 759 Pa·s (Giordano et al., 2008).

3.3. Glass Shard Volatile Content

Dissolved H_2O concentration in the glass shards, mainly hydroxyl groups, range from 0.3% to 0.65 wt % (Figure 6), slightly higher than modern axial PAR glasses (0.15–0.4 wt % H_2O; http://earthchem.org/petdb). CO_2 contents, 120–400 ppm, are elevated compared to average MORB but there are no published CO_2 data for axial PAR samples for comparison. Both H_2O and CO_2 are incompatible species during vapor-undersaturated magmatic fractionation. H_2O is typically only slightly affected by syn-eruptive degassing of seafloor basalts, whereas CO_2 in effusively erupted glasses is significantly degassed and reveals more information on eruption pressures and dynamics than on volatile contents before or during fractionation (Soule et al., 2012). The volatile contents observed are consistent with the glass shards representing evolved samples of the axial magmatic system. The data do not require anomalous volatile enrichments in the parental magma or in the axial magma chamber at the time of eruption. For ridge axis depths > 2 km, the slight elevation in volatile content would not be the main driving force for large explosive eruptions, although higher initial CO_2 cannot be excluded using partially degassed glass shards.

Using the dissolved H_2O and CO_2 data in combination, vapor saturation pressure can be calculated for each shard (Dixon et al., 1995; Newman & Lowenstern, 2002) (Figure 6). Typically, submarine glasses are saturated or oversaturated in volatiles at their eruption depths, because rapid ascent and quenching inhibits degassing; undersaturated samples are quite rare. In the present case, volatiles in the shards define a degassing path from maximum 860 bars (interpreted as a lower bound on axial magma chamber pressure) to minimum 260 bars (interpreted as a maximum eruption depth). Lithostatic pressure of 860 bars corresponds to a minimum storage depth 2.2 km below the seafloor, consistent with the pressure of the calculated liquid line of descent from axial to shard compositions (900 bars). The maximum potential eruption depth estimate, 260 bars, is larger than seafloor pressure at the ridge axis (228 bars) but smaller than seafloor pressure at the present-day core site (278 bars).

3.4. Glass Shard Grain Size and Settling Velocities

The glasses in OC170-26-159 are fine grained and have slow settling velocities. Approximately 50% of the grains are in the 125–250 μm size fraction, with lower concentrations at 63–125 μm (~15%) and 250–500 μm (~35%) (Figure 7a). Very few grains exceed 500 μm. Samples at 150 kyr BP and 156 kyr BP, just below the T2 ash layer, are skewed toward finer grain sizes, perhaps due to preferential downward bioturbation of fine-grained material (Figure 7a). While the grain sizes in the T2 layer and the secondary older deposit are broadly similar, there are subtle differences. Focusing on the highest glass content interval in each layer (134–139 kyr BP and 226–233 kyr BP), the younger interval has a larger proportion of 250–500 μm grains (33.9 ± 0.5%) than the older interval (31.2 ± 0.1%). The younger interval also has a lower percentage of 125–250 μm grains (45.8 ± 0.6% versus 48.4 ± 0.1%). Thus, the T2 interval skews towards slightly coarser grains, despite being deposited when the core site was further from the ridge axis. Settling velocities for blocky pyroclasts in the T2 interval are 1.2 ± 0.3 cm/s (1σ) for 125–150 μm grains, 1.6 ± 0.3 cm/s (1σ) for 150–212 μm, and 1.9 ± 0.3 cm/s (1σ) for 212–250 μm. These values are consistent with published results from other locations (Barreyre et al., 2011) and fall on the low end of the settling velocity spectrum due to their small grain sizes (Figure 8).
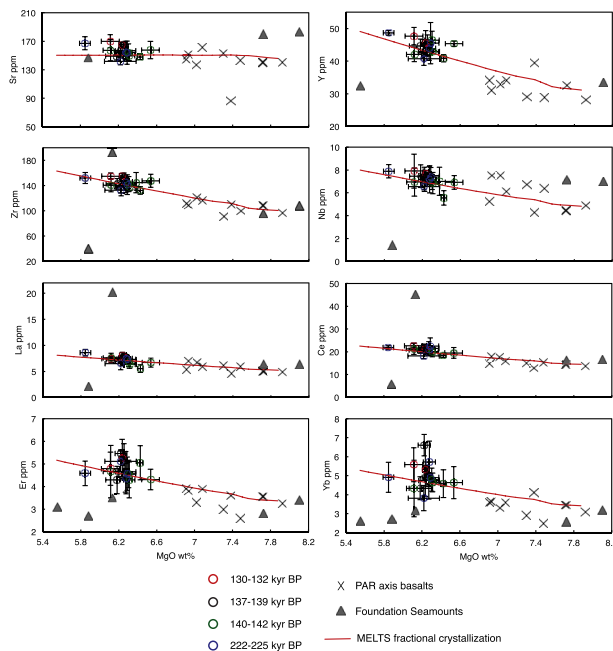
Figure 5. Selected trace element concentrations versus wt % MgO for the basaltic glass shards in OC170-26-159 at four different depth intervals (open circles). Concentrations of incompatible elements are elevated relative to basalts recently erupted from the ridge axis (black X's) (compositions from Hekinian et al., 1997 and Freund et al., 2013). The glass shard compositions fall along a liquid line of descent (red line) calculated using the same pressure, fO_2, and major element composition input values for the MELTS model as in Figure 4. Basalts from the Foundation Seamounts (Hekinian et al., 1997) do not fall on this fractionation trend.

4. Discussion

In the following discussion, we first consider the timing of the T2 layer and the stratigraphic integrity of OC170-26-159. We then detail how the major element, trace element, and volatile content of the ash shards point to an axial source. Next, we discuss how grain settling rates and deep ocean current velocities in the Southeast Pacific can be used to constrain dispersal mechanisms. Finally, we present a hypothesis to account for the T2 layer that integrates the chronological, geochemistry, grain size, and settling velocity results.

4.1. Timing and Stratigraphic Integrity

Perhaps the most interesting aspect of the T2 layer is that it coincides with a glacial termination. The timing is well constrained because the glasses are interspersed with both benthic and planktonic foraminifera that document the oxygen isotopic transition from MIS 6 to MIS 5 (Figure 2). The benthic $\delta^{18}O$ signal at the MIS 6-5 transition is also 1.7‰, indistinguishable from the signal in the benthic $\delta^{18}O$ stack of Lisiecki and Raymo (2005). Together, these observations indicate that OC170-26-159 is stratigraphically sound and that the timing of the main ash layer is well constrained. Both Ti and basalt percentages began to increase prior to T2, indicating that enhanced volcanism preceded the termination (Figure 3).

Analyses of individual benthic foraminifera suggest there is minimal bioturbation in OC170-26-159. Each stratigraphic level during the T2 interval, which encompasses 2–3 cm in core depth (i.e. 2–3 kyr), displays an intrasample $\delta^{18}O$ range of ~0.6‰ (Figure 3). The global benthic $\delta^{18}O$ stack of Lisiecki and Raymo (2005) changes by ~0.2‰ per kyr during T2. Therefore, the expected range of $\delta^{18}O$ values over the age span for each sample would be 0.4–0.6‰, very similar to what we observe. If there were any mixing betweensamples at the beginning and end of T2, we would expect to find the occasional displaced benthic foraminifer, but there is no evidence of displacement in the $\delta^{18}O$ results. The data imply there may have been mixing between adjacent samples, which suggests a bioturbation depth of 2–3 cm. It is unsurprising that bioturbation would cause some signal smoothing given the mean sedimentation rate of 1 cm/kyr, but the timescale of the bioturbation effect (2–3 kyr) is short relative to the duration of the ash layer (~15 kyr). If the T2 layer were due to one eruption subsequently smoothed by bioturbation, the MIS 6-5 transition in $\delta^{18}O$ would not remain intact because the foraminifera are from the same samples and size fraction as the ash itself. It therefore appears that the T2 layer was the product of multiple eruptions rather than a single large event.

The grain size distributions for glasses in OC170-26-159 are similar to those for Gorda Ridge samples more than 3 km from their inferred source, which are clearly skewed toward coarser grain sizes (Figure 7). This suggests that PAR glasses are distal deposits that require lofting of material into the water column and fallout several kilometers downstream. The ash layer near the base of OC170-26-159, deposited when the core was 2–3 km from the axis (Figure 2), may represent routine volcanic activity as described in other locations along the global mid-ocean ridge system (Clague et al., 2009). The T2 layer, however, was deposited when the core site was ~7 km off axis, suggesting it was either the product of unusually large axial eruptions or off-axis events that yielded glasses with grain size and geochemical composition similar to the ash layer near the base of the core.

4.2. An Axial Source

A key uncertainty in interpreting the dispersal of the glass shards is whether they were the product of on- or off-axis volcanism. Ideally, a transect of cores perpendicular to the PAR axis could be used to reconstruct spatial patterns in ash layer thickness and infer the eruptive source. Unfortunately, core OC170-26-159 is the only available core within 40 km of the ridge in this remote region. As a result, we must rely on geochemical analyses of the glasses to assess their provenance.

The volatile content, major element, and trace element analyses of the T2 glasses all point to an axial source. Major element and trace element results fall in a single population with linear trends consistent

Table 1
Initial MELTS Composition

Oxide	Weight %
SiO_2	50.20
TiO_2	1.50
Al_2O_3	14.70
FeO*	9.65
MgO	7.78
CaO	13.50
Na_2O	2.30
K_2O	0.13
Cr_2O_3	0.04
MnO	0.16
H_2O	0.30

Element	ppm
Rb	1.61
Sr	146
Y	31.1
Zr	101
Nb	4.83
Ba	22.1
La	5.23
Ce	14.5
Nd	10.9
Eu	1.51
Dy	4.92
Er	3.36
Yb	3.41
Th	0.35

with derivation from a single magmatic system. The shards have MgO contents lower than basalts from the modern PAR axis and their compositions are consistent with more fractionated members of the same magmatic suite (Figures 4 and 5). Both major and trace element results fall along a modeled liquid line of descent connecting modern axial basalt compositions with the glass shards. The agreement between model results and observations suggests that fractionated axial magmas were the source of the glasses in OC170-26-159. The Foundation Seamounts results typify the highly variable major and trace element concentrations and visibly more scattered fractionation trends of off-axis eruptions compared to the glass shard analyses (Figures 4 and 5). Although the dynamic range of major element variation among seafloor basalts can be small, the variability in trace elements is orders of magnitude larger than the analytical uncertainty. The match between the glass shards and the fractionation trend through the axial glasses in all analyzed trace elements is very unlikely to be coincidental.

Although we cannot completely rule out the possibility that the glass shards erupted from off-axis vents but happen to resemble the products of axial eruptions, this is extremely unlikely. Fast-spreading mid-ocean ridge axes are characterized by persistent axial magma chambers (Detrick et al., 1987; Macdonald & Fox, 1988) that facilitate mixing and homogenization of melts, from highly enriched low-degree or vein-derived melts through to ultra-depleted late fractional melts (Batiza & Niu, 1992; Sinton & Detrick, 1992). Off-axis eruptions typically bypass axial mixing systems and provide windows into the spectrum of variability of mantle melting (Hall & Sinton, 1996; Niu & Batiza, 1997; Niu et al., 2002). The diversity among the Foundation Seamount samples is typical of such unmixed products (Figures 4 and 5). Furthermore, axial magmatic systems have considerable temporal stability because mixing and storage act to smooth out fluctuations in successive batches of magma (Goss et al., 2010; Reynolds et al., 1992). Off-axis systems typically lack such temporal stability, with successive eruptions poorly correlated in composition (Fornari et al., 1988). The glass shards show persistent compositions over a period of several thousand years, based on intercalation with the well-preserved oxygen isotope stratigraphy. Hence, the mean compositions, variability of compositions within each layer, and homogeneity between layers are consistent with derivation from the axial magma system. The homogeneity of the glass shards throughout the core together with the clear difference of this population from the axial magma samples is remarkable. One possibility, though testing it clearly requires more data, is that the axial magma system may have a regulatory feedback mechanism with two stable states, as suggested for the transition from normal basalt to unusually fractionated lavas on the Eastern Lau Spreading Center (Asimow et al., 2005; Eason & Dunn, 2015).

Concentrations of dissolved H_2O in the glasses are elevated with respect to axial basalts, but only to the degree expected for the enrichment of incompatible species due to fractional crystallization of an axial liquid. Saturation pressures calculated from volatile concentrations equate to a maximum pressure consistent with the depth to typical fast-spreading axial magma chambers and with the fractionation model used to reproduce the axial and glass-shard populations. Once again, off-axis eruptions typically do not pass through well-developed storage depths and this would be a coincidence if the glass shards had not fractionated in the axial magmatic system. Furthermore, volatile saturation pressures range down to a minimum consistent with eruption at the relatively shallow axial summit depth and lower than that at the core site. Had these samples erupted on the ridge flanks, they would have been vapor-undersaturated upon eruption, which is rare in submarine glasses. The most likely explanation is that the glass shards erupted from a vent at a shallower water depth than the core site, most likely the PAR axis.

The PAR glasses are evolved not only relative to the PAR axial samples but also compared to samples from other mid-ocean ridge locations. At similar K_2O concentrations (0.18–0.26%), the PAR glasses have distinct MgO values (5.8–6.6% MgO) compared to the compilation of Clague et al. (2009) from several locations in the Pacific, which group primarily from 6.5 to 8.5% MgO. A small batch of samples from the Juan de Fuca Ridge (n = 11) have MgO concentrations overlapping the PAR data, but these are unusual in the broader population (n = 960). Thus, the PAR glasses represent unusually fractionated magmas compared to other settings, which may have contributed to enhanced magmatic viscosity and explosivity during T2.
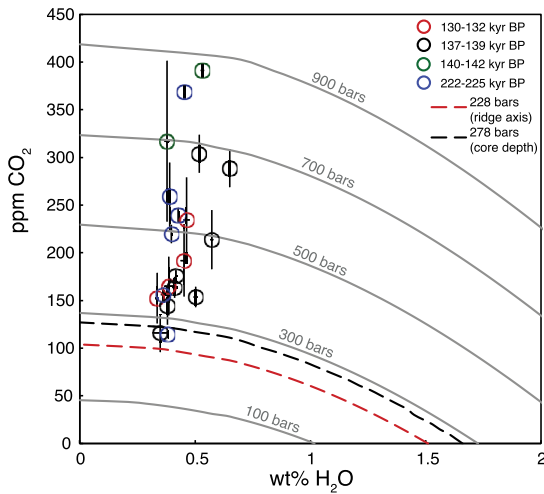
Figure 6. Volatile content for the basaltic glass shards measured using transmission FTIR spectroscopy. Saturation pressure contours were calculated using VolatileCalc 2.0 (Newman & Lowenstern, 2002). Concentrations of H_2O and CO_2 are slightly elevated from that of average MORB. Collectively the glasses record a degassing trend, in which the highest pressure sample records a saturation pressure of 860 bars, and the lowest pressure samples quenched at a maximum of 260 bars. Pressure at the ridge axis and core depth are represented by dashed contours in red and black, respectively. Samples that fall below the core depth equilibrated at a water depth shallower than where the core was retrieved at 2750 m.

4.3. Volcaniclastic Dispersal

Volcaniclastic samples from Loihi Volcano, Axial Seamount, and the Gakkel Ridge have median grain sizes of 340 μm, 360 μm, and 760–1000 μm, respectively (Barreyre et al., 2011), much larger than those at the PAR. Similarly, most of the Gorda Ridge glasses retrieved <3 km from the inferred source have median sizes of 250 μm or larger; only the distal samples are similar in size to the PAR glasses (Figure 7b). These results suggest that coarse grains settled out before reaching the PAR core site. The ash layer at the base of OC170-26-159 was deposited when the core was located 2–3 km off axis, similar to the distal Gorda Ridge sites, and may be the product of routine submarine volcanism (Clague et al., 2009). The T2 layer, however, was deposited 7 km off axis, a distance further than any documented ash layer in the published literature.

Dispersal of volcaniclastic grains depends on buoyant plume rise height, grain settling velocity ($v_{settling}$), and the prevailing deep ocean current speed ($v_{current}$). Assuming that deflection of the ascending plume by currents is minimal, the dispersal distance of a given grain can be estimated using the following equation from Barreyre et al. (2011):

$$distance = \frac{height * v_{current}}{v_{settling}}$$

which shows that dispersal distance is proportional to rise height and current velocity, but inversely proportional to settling velocity. Rearranging and solving for current speed:

$$v_{current} = \frac{distance * v_{settling}}{height}$$

yields the intuitive result that shorter buoyant plume rise heights require greater current velocities to transport grains a given distance. Assuming a dispersal distance of 7 km and a mean settling velocity of 1.6 cm/s, we can estimate the necessary current speed to transport 150–212 μm grains from the PAR axis to the core site. If the rise height was 500 m, the required current velocity is > 20 cm/s. By comparison, a maximum rise height of 2630 m (the water depth of the core minus 120 m to account for the low stand of MIS 6) yields a minimum current velocity of 4 cm/s. Given the uncertainty in the distance from the vent source to the core site (±1.5 km), the minimum velocity ranges from 3 cm/s to 5 cm/s (Figure 9).

Current speeds during T2 are unknown, so we use modern data to constrain the range of possible values. Data from ARGO floats indicate the velocity field near the core site is dominated by mesoscale eddies (Figure 10a) which yield a net westward transport at 39°S (Zhang et al., 2014). Given that OC170-26-159 is located west of the ridge axis and that eddies persist on the timescale of weeks to months (compared to a fallout time for the grains of hours to days), eddies are likely the primary means by which volcaniclastics were transported westward. Ninety percent of the current speed estimates at 2000 db (~2000 m water depth) are less than 3.1 cm/s, with a median value of 1.2 cm/s (Figure 10b). By comparison, 95% of the values at 1000 db are less than 4.6 cm/s, with a median of 2.1 cm/s. Thus, the required current velocity of ~20 cm/s for a rise height of 500 m is far higher than any value in the modern dataset. A rise height of 1500 m, which would reach to ~1000 m water depth, requires a current velocity ≥ 5.5 cm/s, which is observed in only 2% of the ARGO-derived velocities at 1000 db. On the other hand, rise heights of 2000 m yield implied current velocities ≥ 4 cm/s, which overlaps with the high end of observed values (Figure 10b). It therefore appears that the buoyant plume associated with the T2 layer occupied most of the water column.

4.4. A Hypothetical Mechanism

The preceding discussion outlines the case for an interval of anomalous volcanism along the PAR. Given the evolved nature of the PAR glasses, a period of abnormally low heat flux to the ridge axis is required for the axial magma reservoir to cool, fractionate and produce lavas consistent with the shard composition. We speculate that rising sea level prior to MIS 7 suppressed melt generation and subsequent melt flux to the
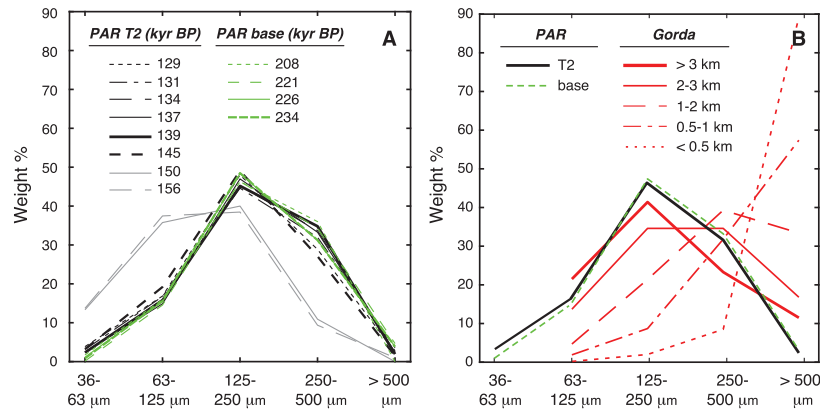
Figure 7. Grain size distributions for pyroclastic debris on the Pacific-Antarctic Ridge and the Gorda Ridge. (**a**) Grain size distributions for PAR samples where basaltic glass composed >3% of the total weight. Labels represent time in kyr BP for each sample. Grain sizes are similar for the T2 interval and the base of the core, with the exception of data at 150 kyr BP and 156 kyr BP (gray), which are skewed towards finer grain sizes. (**b**) Mean grain size distributions for the T2 interval (black) and base of the PAR core (green) compared to results from the Gorda Ridge (red) (data from Clague et al., 2009). The grain size distribution for the Gorda Ridge results furthest from the lava flow (> 3 km) are similar to those for the PAR. The right-hand plot does not include Gorda Ridge data for 36–63 μm because it was dominated by terrigenous material (Clague et al., 2009).

ridge axis (see Lund & Asimow, 2011), allowing fractionation to occur (Figure 11b). The modeled evolution of magma suggests that the axial chamber cooled from 1190 to 1150°C, which corresponds to a ~30x increase in magma viscosity and an increase in the magmatic volatile content of ~25%, both of which would facilitate explosive volcanism. Thermal modeling of the balance between magmatic heat input and hydrothermal cooling at mid-ocean ridges suggests that magma chamber depth and temperature is quite sensitive to variations in magmatic heat input of this magnitude (e.g., Morgan & Chen, 1993).

Falling sea level at the transition to MIS 6 would enhance decompression melting in the upper mantle compared to the preceding minimum (Figure 11c). The delayed arrival of this melt at the ridge axis could have re-mobilized the fractionated melt, thereby initiating volcanism. To explain the observations, it would be necessary that the products of these events be dominated by the stored, fractionated melt and not by the fresh input. Such behavior has been documented in mafic-felsic magmatic systems where large density contrasts suppress magma mixing (e.g., Bachmann et al., 2002). We speculate that the associated eruptions yielded sufficient heat to create plumes capable of lofting fine-grained volcaniclastics nearly the full height of the water column, enabling transport of the grains to distal off-axis locations (Figure 11d). While cooler, more fractionated lava may be less efficient per unit mass at heating plume water, the greatly increased eruption rate associated with episodic events would more than overcome this effect. In the proposed scenario, rising and falling sea level each play key roles in driving anomalous volcanism, with the former
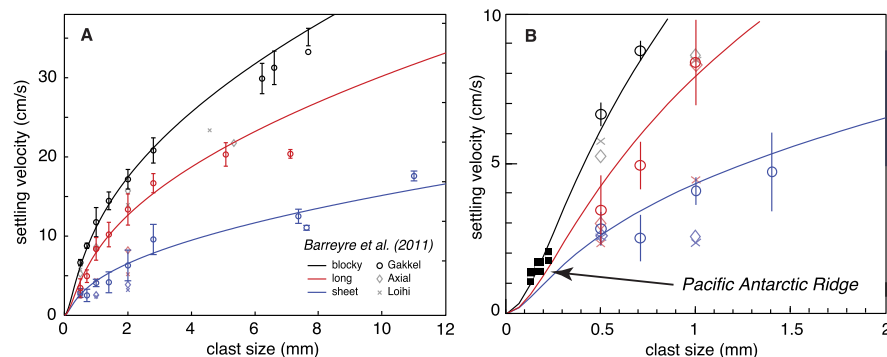
Figure 8. Settling velocities for the PAR glass shards compared to published data. (**a**) Figure from Barreyre et al. (2011) showing settling velocities for volcaniclastic grains from the Gakkel Ridge, Axial Seamount, and Loihi Volcano, including blocky, long and sheet morphologies. (**b**) Same as panel A, except focused on the 0–2 mm size range and including new results from the PAR for blocky grains at three different size fractions: 125–150 μm, 150–212 μm, and 212–250 μm. Error bars for all results are $\pm 1\sigma$.
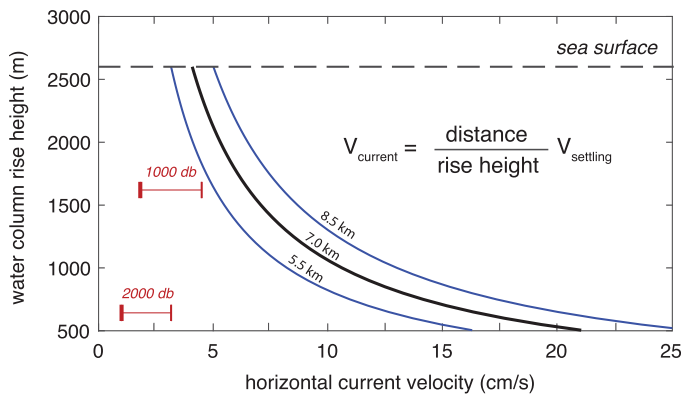
Figure 9. Plume rise height and current speed combinations required to transport grains with 1.6 cm/s settling velocity from the PAR to the core site at 140 kyr BP. The black curve reflects the distance from the central ridge axis (7 km), while the blue curves span the full axial plateau distance (5.5–8.5 km). At 2000 db, 95% of ARGO current speed estimates are < 3.1 cm/s (thin vertical red line), with a median value of 1.2 cm/s (thick vertical red line). At 1000 db, 95% of the ARGO current speeds are < 4.6 cm/s, with a median of 2.1 cm/s (Figure 10b). Rise heights less than 2000 m require unrealistically large current velocities for the deep Southeast Pacific.

causing melt starvation and enhanced magma viscosity, while the latter triggers eruptions through enhanced melt flux.

The delay between falling sea level at the start of MIS 6 and T2 is approximately 50 kyr. Assuming an average melt origin depth of 50 km (Key et al., 2013), these results imply a melt extraction velocity of ~1 m/yr, which is consistent with the rate implied by U/Th disequilibrium (Kelemen et al., 1997) but slower than estimates from Iceland (Maclennan et al., 2002). Extraction rates previously estimated from hydrothermal records along the EPR (2–5 m/yr; Lund et al., 2016) assumed that Termination 1 anomalies were associated with the MIS 2-1 transition. If instead they were related to the MIS 5-4 drop in sea level, the implied migration rate for EPR sites would also be ~1 m/yr, assuming no significant lags associated with crustal filtering or hydrothermal processes. We recognize that this aspect of the proposed model apparently requires special tuning in order to deliver the increased melt pulse at the right time; additional well-dated pyroclastic records from ridge-proximal locations are necessary to evaluate whether the lag time implied by the PAR results is representative of other ridges.

4.5. Prospects

Given the unique nature of the PAR results, it is logical to ask whether there are similar records available from other locations. The short answer is, most likely, no. For a core to preserve dateable volcanic ash layers it needs to meet three key criteria: (1) the water depth must be above the CCD to preserve the foraminifera required for oxygen isotope dating; (2) the core must be within ~10 km of the ridge axis at the time of the eruption, which is the maximum distance that fine grained volcaniclastics can be transported given the depth of mid-ocean ridges and typical deep ocean current speeds; and (3) the core must be sufficiently long that it penetrates nearly to basement. The last requirement is the result of low sedimentation rates in the open ocean (~1 cm/kyr or less) and the age of ocean crust within 10 km of a ridge axis. Assuming a global average half-spreading rate of 25 m/kyr (DeMets et al., 1994), the crust within 10 km of a ridge axis will typically be less than 400 kyr old and bear sediment less than 4 m thick, assuming no erosion or re-deposition by bottom currents. At locations closer than 10 km, the accumulated sediment will be thinner; as a result, any ash deposits will exist at the base the sediment column, within a few meters or less of the oceanic crust.

Tailoring the expected sediment thickness to spreading rate, we used the above criteria to search for cores in existing repositories that may contain ash layers associated with the last five glacial terminations. Out of 18,600 gravity and piston cores in the repositories at Lamont-Doherty Earth Observatory, Oregon State University, Woods Hole Oceanographic Institution, and the University of Rhode Island, ~130 fall within 50 km of a ridge axis (i.e., <1%). Of these cores, only 30 meet the criteria of axial proximity, water depth, and core length. Visual inspection of the cores at the four repositories suggests that ~20 have been sufficiently well preserved since they were collected to warrant sampling. It is likely that only half will have a coherent oxygen isotope stratigraphy, which is the yield we have observed in archived cores from the EPR. We therefore anticipate that about 10 of the 18,600 cores at four of the largest repositories in the U.S. (~0.05%) will be useful for reconstructing submarine volcanism.

While examination of existing cores should proceed, the historical bias in avoiding coring near ridges will make it difficult to determine whether the T2 ash layer in OC170-26-159 is a unique find or a representative feature of glacial terminations. The odds of success would be vastly higher for a targeted sampling cruise aimed specifically at sites that satisfy the selection criteria. Such an effort will be needed, not only to assess ash dispersal patterns on the PAR, but also at ridges with different spreading rate, magma supply, and other key variables. For example, if the mechanism we propose is correct then one might anticipate an ash layer during Termination 1 in core OC170-26-159. During T1, however, the core site would have been 13 km off-axis, further than the maximum dispersal distance for fine grained ashes. A key test of our hypothesis would to be to examine a core that was ~7 km off-axis during T1, similar to the distance of OC170-26-159 during T2.
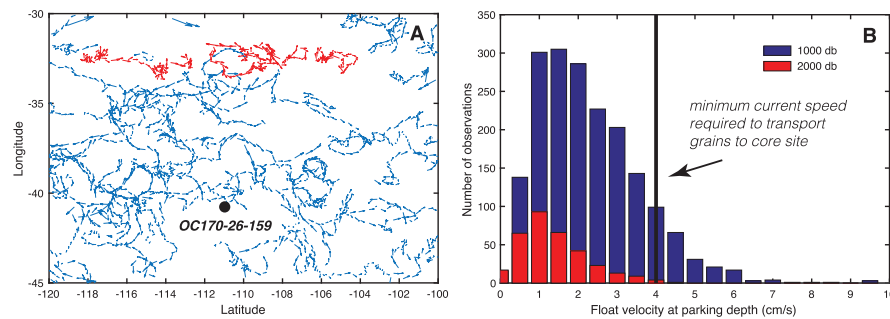
Figure 10. ARGO float velocities in the region of OC170-26-159 (http://apdrc.soest.hawaii.edu/projects/yomaha). (**a**) Current vectors showing mesoscale (100–200 km) eddies dominate the flow field at 1000 db (blue arrows) and 2000 db (red arrows). (**b**) Histograms of current velocity at 1000 db (blue) and 2000 db (red). The minimum horizontal current speed of 4 cm/s is based on a plume rise height of 2600 m and mean grain settling velocity of 1.6 cm/s. Shorter rise heights require faster horizontal current velocities (Figure 9).
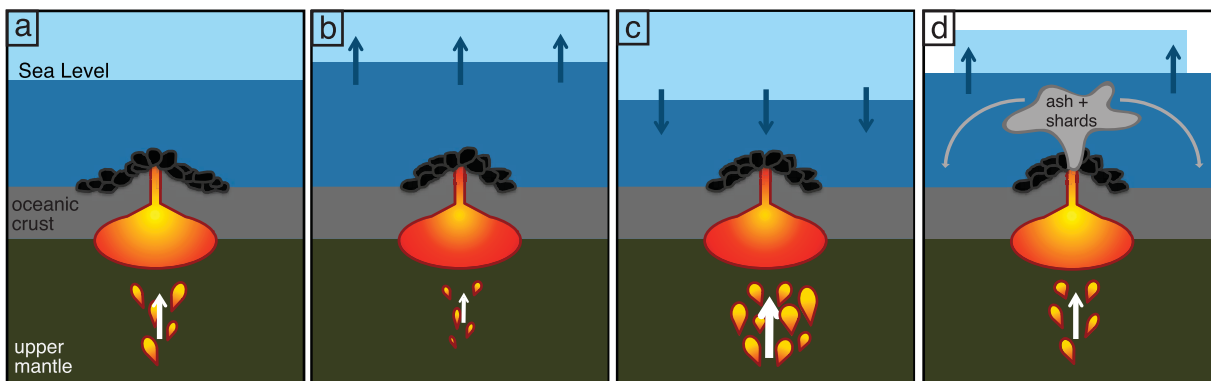
Figure 11. Schematic diagram showing the sequence of sea level changes and magmatic responses that may lead to Strombolian eruptions. (**a**) The PAR during a period of relatively stable sea level, with an unmodulated melt flux and magma chamber of normal MORB composition. (**b**) 190–220 kyr BP: Rising and high sea level suppresses melting beneath the ridge axis, leading to a decreased melt flux into the axial magma chamber. With a less voluminous source of new melt, the axial chamber cools slightly and fractionates to create a more viscous, evolved lava. (**c**) 180–190 kyr BP: Sea level decreases rapidly, stimulating a pulse of melting at depth. The melt percolates upward from the melting depth before it reaches the axial magma chamber, so it does not yet affect eruption style or composition. (**d**) 120–140 kyr BP: Melt flux to the ridge axis is high when the melt pulse reaches the axial magma chamber. This remobilizes the viscous fractionated magma in a series of eruptions.

5. Conclusions

The ash layer in core OC170-26-159 is unlike any deposit described to date, given its timing, geochemistry, and distance from the PAR axis at the time of deposition. The deposit appears to precede Termination 2 and the shard morphology is consistent with Strombolian style eruptive events. Geochemical analyses indicate the glasses were derived from unusually fractionated magmas with high viscosity that likely contributed to the explosivity of the associated eruptions. The homogenous nature of the major and trace element results points to an axial magma chamber origin where successive batches of melt can be well mixed prior to eruption. The match between the shard compositions and a fractionation model through axial samples from the PAR is also consistent with an axial source for the T2 layer.

Dispersal of the T2 glasses likely occurred through lofting of volcaniclastic debris in buoyant seawater plumes and fallout to off-axis locations, with a length-scale dictated by plume rise height, grain settling velocity, and deep ocean current speeds. The fine grain size and slow settling velocity of the T2 glasses likely facilitated their transport to the core site; a rise height of $\sim$ 2 km is required to access parts of the water column with adequate current velocities to transport the glasses 7 km off axis. A second ash layer near the base of the core with lower glass concentrations was deposited when the site was 2–3 km from the ridge axis, consistent with the dispersal distances at other mid-ocean ridge locations (Clague et al., 2009). Thus, the volcanism associated with the T2 layer was unusual not only in terms of timing but also in terms of dispersal. Detailed reconstruction of ash layer thicknesses based on a suite of well-dated sediment

cores will be necessary to fully assess dispersal patterns. The probability of finding similar archives in core repositories is low given that only a tiny number of existing cores have the necessary length and proximity to a ridge crest to capture ash layers. The most promising avenue will therefore be through targeted coring expeditions tailored specifically to find volcaniclastic deposits in ridge proximal locations.

Our study of core OC170-26-159 on the Pacific Antarctic Ridge was motivated by the question of links between mid-ocean ridge magmatic and hydrothermal activity, on the one hand, and glacially-driven sea level variations, on the other. In this context, the occurrence of unusual volcanic activity preceding a glacial termination is intriguing. We present a hypothetical sea level mechanism that may explain the link between these phenomena. Our intent is to motivate further studies of axial glass deposits to test this hypothesis.

References

Adkins, J. F., McIntyre, K., & Schrag, D. P. (2002). The salinity, temperature, and delta O-18 of the glacial deep ocean. *Science*, *298*(5599), 1769–1773.

Asimow, P. D., Dixon, J. E., & Langmuir, C. H. (2004). A hydrous melting and fractionation model for mid-ocean ridge basalts: Application to the Mid-Atlantic Ridge near the Azores. *Geochemistry, Geophysics, Geosystems*, *5*, Q01E16. https://doi.org/10.1029/2003GC000568

Asimow, P. D. & Ghiorso, M. S. (1998). Algorithmic modifications extending Melts to calculate subsolidus phase relations. *American Mineralogist*, *83*(9–10), 1127–1132.

Asimow, P. D., Langmuir, C. H., & the Kilo Moana 0417 Shipboard Science Party. (2005). Effect of water on magma and crustal density: Highly fractionated lavas in the Lau Basin and other wet spreading centers. 2005 Goldschmidt Conference, Moscow Idaho. *Geochimica et Cosmochimica Acta*, *69* (10 Suppl.), A149.

Bachmann, O., Dungan, M. A., & Lipman, P. W. (2002). The Fish Canyon Magma Body, San Juan Volcanic Field, Colorado: Rejuvenation and Eruption of an Upper-Crustal Batholith. *Journal of Petrology*, *43*(8), 1469–1503. https://doi.org/10.1093/petrology/43.8.1469

Barreyre, T., Soule, S. A., & Sohn, R. A. (2011). Dispersal of volcaniclasts during deep-sea eruptions: Settling velocities and entrainment in buoyant seawater plumes. *Journal of Volcanology and Geothermal Research*, *205*(3–4), 84–93. https://doi.org/10.1016/j.jvolgeores.2011.05.006

Batiza, R., & Niu, Y. (1992). Petrology and magma chamber processes at the East Pacific Rise ∼ 9°30′N. *Journal of Geophysical Research*, *97*(B5), 6779–6797.

Briais, A., Ondréas, H., Klingelhoefer, F., Dosso, L., Hamelin, C., & Guillou, H. (2009). Origin of volcanism on the flanks of the Pacific-Antarctic Ridge between 41°30′S and 52°S. *Geochemistry, Geophysics, Geosystems*, *10*(9), Q09001.

Clague, D. A., Davis, A. S., & Dixon, J. E. (2003). Submarine Strombolian eruptions on the Gorda mid-ocean ridge. *AGU Geophysical Monograph Series*, *140*, 111–128.

Clague, D. A., Paduan, J. B., & Davis, A. S. (2009). Widespread strombolian eruptions of mid-ocean ridge basalt. *Journal of Volcanology and Geothermal Research*, *180*(2–4), 171–188. https://doi.org/10.1016/j.jvolgeores.2008.08.007

Costa, K. M., McManus, J. F., Middleton, J. L., Langmuir, C. H., Huybers, P. J., Winckler, G., & Mukhopadhyay, S. (2017). Hydrothermal deposition on the Juan de Fuca Ridge over multiple glacial-interglacial cycles. *Earth and Planetary Science Letters*, *479*, 120–132.

Crowley, J. W., Katz, D., Huybers, P., Langmuir, C., & Park, S. (2015). Glacial cycles drive variations in production of oceanic crust. *Science*, *347*(6227), 1237–1240.

Demets, C., Gordon, R. G., Argus, D. F., & Stein, S. (1994). Effect of recent revisions to the geomagnetic reversal time-scale on estimates of current plate motions. *Geophysical Research Letters*, *21*(20), 2191–2194.

Detrick, R. S., Buhl, P., Vera, E., Mutter, J., Orcutt, J., Madsen, J., & Brocher, T. (1987). Multichannel seismic imaging of a crustal magma chamber along the east pacific rise. *Nature*, *326*(6108), 35–41.

Dixon, J. E., Stolper, E. M., & Holloway, J. R. (1995). An experimental study of water and carbon dioxide solubilities in mid-ocean ridge basaltic liquids. Part I: Calibration and solubility models. *Journal of Petrology*, *36*(6), 1607–1631.

Dunk, R. M., & Mills, R. A. (2006). The impact of oxic alteration on plume-derived transition metals in ridge flank sediments from the east pacific rise. *Marine Geology*, *229*(3–4), 133–157.

Eason, D. E., & Dunn, R. A. (2015). Petrogenesis and structure of oceanic crust in the Lau back-arc basin. *Earth and Planetary Science Letters*, *429*, 128–138.

Ferguson, D. J., Li, Y., Langmuir, C. H., Costa, K. M., McManus, J. F., Huybers, P., & Carbotte, S. M. (2017). A 65 k.y. time series from sediment-hosted glasses reveals rapid transitions in ocean ridge magmas. *Geology*, *45*(6), 491–494. https://doi.org/10.1130/G38752.1.

Fine, G., & Stolper, E. (1985). The speciation of carbon dioxide in sodium aluminosilicate glasses. *Contributions to Mineralogy and Petrology*, *91*(2), 105–121. https://doi.org/10.1007/BF00377759

Fornari, D. J., Perfit, M. R., Allan, J. F., Batiza, R., Haymon, R., Barone, A., et al. (1988). Geochemical and structural studies of the Lamont seamounts: Seamounts as indicators of mantle processes. *Earth and Planetary Science Letters*, *89*(1), 63–83. https://doi.org/10.1016/0012-821X(88)90033-7

Freund, S., Beier, C., Krumm, S., & Haase, K. M. (2013). Oxygen isotope evidence for the formation of andesitic-dacitic magmas from the fast-spreading Pacific-Antarctic Rise by assimilation-fractional crystallisation. *Chemical Geology*, *347*, 271–283. https://doi.org/10.1016/j.chemgeo.2013.04.013

Ghiorso, M. S., & Sack, R. O. (1995). Chemical mass transfer in magmatic processes IV. A revised and internally consistent thermodynamic model for the interpolation and extrapolation of liquid-solid equilibria in magmatic systems at elevated temperatures and pressures. *Contributions to Mineralogy and Petrology*, *119*(2–3), 197–212. https://doi.org/10.1007/BF00307281

Giordano, D., Russell, J. K., & Dingwell, D. B. (2008). Viscosity of magmatic liquids: A model. *Earth and Planetary Science Letters*, *271*(1–4), 123–134. https://doi.org/10.1016/j.epsl.2008.03.038

Goff, J. A. (2015). Comment on "glacial cycles drive variations in the production of oceanic crust". *Science*, *349*(6252), 1065. https://doi.org/10.1126/science.aab2350

Goss, A. R., Perfit, M. R., Ridley, W. I., Rubin, K. H., Kamenov, G. D., Soule, S. A., et al. (2010). Geochemistry of lavas from the 2005–2006 eruption at the east pacific rise, 9°46′N-9°56N: Implications for ridge crest plumbing and decadal changes in magma chamber compositions. *Geochemistry, Geophysics, Geosystems*, *11*(5), n/a. https://doi.org/10.1029/2009GC002977

Hall, L. S., & Sinton, J. M. (1996). Geochemical diversity of the large lava field on the flank of the East Pacific Rise at 8°17'S. *Earth and Planetary Science Letters*, *142*(1–2), 241–251.

Hekinian, R., Stoffers, P., Ackermand, D., Révillon, S., Maia, M., & Bohn, M. (1999). Ridge-hotspot interaction: The Pacific-Antarctic ridge and the Foundation Seamounts. *Marine Geology*, *160*(3–4), 199–223. https://doi.org/10.1016/S0025–3227(99)00027-4

Hekinian, R., Stoffers, P., Devey, C., Ackerman, D., Hémond, C., O'Connor, J., Binard, N., & Maia, M. (1997). Intraplate versus ridge volcanism on the Pacific-Antarctic Ridge near 37°S–111°W, *Journal of Geophysical Reseasrch*, *102*(B6), 12265–12286.

Huybers, P., & Langmuir, C. (2009). Feedback between deglaciation, volcanism, and atmospheric CO$_2$. *Earth and Planetary Science Letters*, *286*(3–4), 479–491.

Kelemen, P. B., Hirth, G., Shimizu, N., Spiegelman, M., & Dick, H. J. B. (1997). A review of melt migration processes in the adiabatically upwelling mantle beneath oceanic spreading ridges. *Philosophical Transactions of the Royal Society of London, Series A*, *355*(1723), 283–318.

Key, K., Constable, S., Liu, L., & Pommier, A. (2013). Electrical image of passive mantle upwelling beneath the northern East Pacific Rise. *Nature*, *495*(7442), 499–502.

Klingelhoefer, F., Ondréas, H., Briais, A., Hamelin, C., & Dosso, L. (2006). New structural and geochemical observations from the Pacific-Antarctic Ridge between 52°45'S and 41°. *Geophysical Research Letters*, *33*(21), 15'S. https://doi.org/10.1029/2006GL027335

Lebedev, K., Yoshinari, H., Maximenko, N., & Hacker, P. (2007). YoMaHa 2007: Velocity data assessed from trajectories of ARGO floats at parking level and at the sea surface (IPRC Tech. Note No. 4(2)). International Pacific Research Center.

Lisiecki, L. E., & Raymo, M. E. (2005). A Pliocene-Pleistocene stack of 57 globally distributed benthic delta O-18 records. *Paleoceanography*, *20*(1), 17.

Lund, D. C., & Asimow, P. D. (2011). Does sea level influence mid-ocean ridge magmatism on Milankovitch timescales? *Geochemistry Geophysics Geosystems*, *12*(12), Q12009.

Lund, D. C., Asimow, P. D., Farley, K. A., Rooney, T. O., Seeley, E., Jackson, E. W., & Durham, Z. M. (2016). Enhanced east pacific rise hydrothermal activity during the last two glacial terminations. *Science*, *351*(6272), 478–482. https://doi.org/10.1126/science.aad4296

Macdonald, K. C., & Fox, P. J. (1988). The axial summit graben and cross-sectional shape of the East Pacific Rise as indicators of axial magma chambers and recent volcanic eruptions. *Earth and Planetary Science Letters*, *88*(1–2), 119–131. https://doi.org/10.1016/0012-821X(88)90051-9.

Maclennan, J., Jull, M., McKenzie, D., Slater, L., & Gronvold, K. (2002). The link between volcanism and deglaciation in Iceland. *Geochemistry Geophysics Geosystems*, *3*(11), 1062. https://doi.org/10.1029/2001GC000282

Middleton, J. L., Langmuir, C. H., Mukhopadhyay, S., McManus, J. F., & Mitrovica, J. X. (2016). Hydrothermal iron flux variability following rapid sea level changes. *Geophysical Research Letters*, *43*(8), 3848–3856.

Morford, J. L., & Emerson, S. (1999). The geochemistry of redox sensitive trace metals in sediments. *Geochimica et Cosmochimica Acta*, *63*(11–12), 1735–1750.

Morgan, J. P., & Chen, Y. J. (1993). The genesis of oceanic crust: Magma injection, hydrothermal circulation, and crustal flow. *Journal of Geophysical Research: Solid Earth*, *98*(B4), 6283–6297. https://doi.org/10.1029/92JB02650

Newman, S., & Lowenstern, J. B. (2002). VOLATILECALC: A silicate melt-H$_2$O-CO$_2$ solution model written in visual basic for excel. *Computers and Geosciences*, *28*(5), 597–604. https://doi.org/10.1016/S0098-3004(01)00081-4

Niu, Y., & Batiza, R. (1997). Trace element evidence from seamounts for recycled oceanic crust in the eastern Pacific mantle. *Earth and Planetary Science Letters*, *148*(3–4), 471–483.

Niu, Y., Regelous, M., Wendt, I. J., Batiza, R., & O'hara, M. J. (2002). Geochemistry of near-EPR seamounts: Importance of source vs. process and the origin of enriched mantle component. *Earth and Planetary Science Letters*, *199*(3–4), 327–345. https://doi.org/10.1016/S0012-821X(02)00591-5

Olive, J., Behn, M. D., Ito, G., Buck, W. R., Escartìn, J., & Howell, S. (2015). Sensitivity of seafloor bathymetry to climate-driven fluctuations in mid-ocean ridge magma supply. *Science*, *350*(6258), 310–313. https://doi.org/10.1126/science.aad0715

Ostermann, D. R., & Curry, W. B. (2000). Calibration of stable isotopic data: An enriched delta O-18 standard used for source gas mixing detection and correction. *Paleoceanography*, *15*(3), 353–360.

Portner, R. A., Clague, D. A., Helo, C., Dreyer, B. M., & Paduan, J. B. (2015). Contrasting styles of deep-marine pyroclastic eruptions revealed from axial seamount push core records. *Earth and Planetary Science Letters*, *423*, 219–231. https://doi.org/10.1016/j.epsl.2015.03.043

Ryan, W. B. F., Carbotte, S. M., Coplan, J. O., O'Hara, S., Melkonian, A., Arko, R., et al. (2009). Global multi-resolution topography synthesis. *Geochemistry Geophysics Geosystems*, *10*, 9.

Reynolds, J. R., Langmuir, C. H., Bender, J. F., Kastens, K. A., & Ryan, W. B. F. (1992). Spatial and temporal variability in the geochemistry of basalts from the East Pacific Rise. *Nature*, *359*(6395), 493–499.

Rubin, K. H., Smith, M. C., Bergmanis, E. C., Perfit, M. R., Sinton, J. M., & Batiza, R. (2001). Geochemical heterogeneity within mid-ocean ridge lava flows: Insights into eruption, emplacement and global variations in magma generation. *Earth and Planetary Science Letters*, *188*(3–4), 349–367. https://doi.org/10.1016/S0012-821X(01)00339-9

Sinton, J. M., & Detrick, R. S. (1992). Mid-ocean ridge magma chambers. *Journal of Geophysical Research*, *97*(B1), 197–216.

Sohn, R. A., Willis, C., Humphris, S., Shank, T. M., Singh, H., Edmonds, H. N., et al. (2008). Explosive volcanism on the ultraslow-spreading Gakkel Ridge, Arctic Ocean. *Nature*, *453*(7199), 1236–1238. https://doi.org/10.1038/nature07075

Soule, S. A., Nakata, D. S., Fornari, D. J., Fundis, A. T., Perfit, M. R., & Kurz, M. D. (2012). CO$_2$ variability in mid-ocean ridge basalts from syn-emplacement degassing: Constraints on eruption dynamics. *Earth and Planetary Science Letters*, *327–328*, 39–49.

Tolstoy, M. (2015). Mid-ocean ridge eruptions as a climate valve. *Geophysical Research Letters*, *42*(5), 1346–1351. https://doi.org/10.1002/2014GL063015

Zhang, Z., Wang, W., & Qiu, B. (2014). Oceanic mass transport by mesoscale eddies. *Science*, *345*(6194), 322–324. https://doi.org/10.1126/science.1252418